Citation information: DOI: 10.1109/JLT.2025.3647694, Journal of Lightwave Technology

Experimental Demonstration of Bending Eavesdropping Detection in Optical Communications using a Physics-Informed Convolutional Network

Wenshuai Qin, Xiaoxue Gong, Weigang Hou, Lu Gan, Lei Guo

***Abstract*—This paper proposes a physics-informed convolutional network (PICN) scheme to detect bending eavesdropping attacks in dual-polarization coherent optical communication systems. We present a theoretical model for optical signal transmission under bending eavesdropping, analyzing the impact of bending eavesdropping on fiber physical characteristics such as dispersion and nonlinear effect. These physical characteristics are embedded into a convolutional neural network (CNN) to construct PICN, which automatically captures subtle variations of the signal features under bending eavesdropping. To validate the effectiveness of the scheme, we first develop an eavesdropping experimental platform in an 80 km 168 Gbps dual-polarization quadrature phase shift keying (QPSK) coherent optical communication system. Polarization data are then collected under normal transmission, 10.8 mm and 15 mm bending radius. Finally, the detection performance of four classifiers including PICN, random forest (RF), support vector machine (SVM), and K-nearest neighbor (KNN) are evaluated at single and mixed bending radii. Experimental results demonstrate that PICN achieves detection accuracies of 100%, 98.53%, and 99.02% under 10.8 mm, 15 mm, and mixed bending radii, respectively. Our work provides novel theoretical foundations and innovative perspectives for bending eavesdropping detection in optical fiber communication systems.**

***Index Terms*—Bending eavesdropping detection, secure optical communications physics-informed convolutional network.**

I. INTRODUCTION

FIBER communication is the foundational element of information transmission, responsible for carrying over 90% of global internet data traffic [1], [2], [3], [4], [5], [6]. Since optical fibers are insulating media with high resistance to electromagnetic interference (EMI) and optical signals are strictly confined within the waveguide structure with near-zero leakage during propagation, they were once considered highly secure. However, with the emergence of various advanced eavesdropping methods such as fiber bending, V-groove cutting, and grating scattering, it has been demonstrated that optical fibers are vulnerable to eavesdropping [7], [8], [9], [10]. Among these methods, bending eavesdropping has attracted significant attention due to its low implementation cost and strong concealment. This technique is achieved by stripping the protective coating of the fiber, bending it with a specific curvature radius, and exploiting the mode coupling induced by the macro-bending effect to extract signals [11], [12]. Furthermore, optical signal power attenuation caused by bending eavesdropping is typically below the system detection threshold, making it difficult for existing optical network monitoring devices to detect effectively [13], [14], [15]. Meanwhile, the transmission rate of optical signals in fibers can reach terabit-level speeds. This implies that even brief eavesdropping on the fiber results in massive data leakage. Therefore, it is important to explore detection methods for bending eavesdropping attacks.

In the context of detecting eavesdropping, existing research mainly focuses on machine learning (ML) methods [16], [17], [18], [19], [20]. Reference [21] proposed a long short-term memory (LSTM) based detection scheme for bending eavesdropping, achieving 95.83% accuracy by using smoothed time domain data. Similarly, Reference [22] introduced a convolutional neural network (CNN) approach for optical splitting eavesdropping detection, which attained 97% accuracy at 5% split ratio through the combination of eye diagram analysis and optical performance monitoring (OPM) metrics. Our previous work proposed a optical splitting eavesdropping detection scheme based backpropagation neural network (BPNN) [23]. By utilizing single-polarization spectra as the model input achieved 99% detection accuracy. However, its detection performance in dual-polarization coherent optical communication systems still requires further investigation. Notably, existing research exhibits two limitations. First, it lacks theoretical modeling of bending eavesdropping mechanisms, which makes it difficult to analyze the specific impact of eavesdropping on optical signal transmission. More importantly, existing neural network architectures in prior work have not adequately incorporated the physical characteristics of optical fiber channels. Specifically, existing detection models ignore the impacts of physical parameters such as dispersion and nonlinear effect. This disconnection between physical mechanisms and data-

This work was supported in part by the National Key Research and Development Program of China under Grant 2023YFB2905900, in part by the National Natural Science Foundation of China under Grants U24B20134, 62222103, in part by the Chongqing Municipal Education Commission under Grants KJZD-K202400608.

Wenshuai Qin, Xiaoxue Gong (Corresponding author), Weigang Hou, Lei Guo are with the School of Communications and Information Engineering, Chongqing University of Posts and Telecommunications, Chongqing 400065, China (e-mail: gongxx@cqupt.edu.cn).

Wenshuai Qin, Xiaoxue Gong, Weigang Hou, Lei Guo are with the Institute of Intelligent Communications and Network Security, Chongqing University of Posts and Telecommunications, Chongqing 400065, China.

Lu Gan is with Department of Electrical and Computer Engineering, Brunel University London, UB8 3PH, U.K.

driven may constrain both the accuracy and generalization capability of models.

To address the above challenges, this paper proposes a physics-informed convolutional network (PICN) detection scheme for bending eavesdropping attacks in dual-polarization coherent optical communication systems. First, we present a theoretical model for optical signal transmission under bending eavesdropping and analyze the impacts of fiber dispersion and nonlinear effects on the signal. Subsequently, these physical characteristics are integrated into CNN to propose the PICN model with dispersion and nonlinear modules. This integration enables the model to accurately simulate optical signal transmission characteristics in fiber channels, which captures subtle variations of signal feature under bending eavesdropping. Finally, to verify the effectiveness of the scheme, an 80 km, 168 Gbps dual-polarization quadrature phase shift keying (QPSK) coherent optical communication experimental platform is constructed. The performance of four algorithms (PICN, random forest (RF), support vector machine (SVM), and K-nearest neighbor (KNN)) is evaluated for detecting bending eavesdropping. The experimental results show that PICN achieves detection accuracies of 100%, 98.53%, and 99.02% under 10.8 mm, 15 mm, and mixed bending radii, respectively. Overall, this work integrates physical properties with data-driven analysis technology and provides an innovative solution for bending eavesdropping detection in optical communication systems.

The remainder of this paper is organized as follows. Section II presents the optical signal transmission model under bending eavesdropping. Section III details the bending eavesdropping detection scheme based on PICN. Section IV describes the experimental setup and data collection under bending eavesdropping. Section V presents a comprehensive evaluation of the PICN model detection performance under various bending conditions. Finally, conclusions are provided in Section VI.

II. OPTICAL SIGNAL TRANSMISSION MODEL UNDER FIBER BENDING EAVESDROPPING

To explore the effect of bending eavesdropping on the physical characteristics of optical signal transmission, we construct a transmission model of a dual-polarization coherent optical communication system under bending eavesdropping. In such systems, light waves propagate along two orthogonal polarization directions, and the transmission process is described by a partial differential equation [24].

$$\begin{aligned}
&\frac{\partial^2 E_x\left(x,y,z,\omega-\omega_0\right)}{\partial x^2}+\frac{\partial^2 E_x\left(x,y,z,\omega-\omega_0\right)}{\partial y^2}\\
&+\frac{\partial^2 E_x\left(x,y,z,\omega-\omega_0\right)}{\partial z^2}\\
&+\mu_0\varepsilon_0\left[1+\chi_{xx}^{(1)}+\frac{3}{4}\chi_{xxxx}^{(3)}\left|E_x\left(x,y,z,t\right)\right|^2\right]\cdot\\
&\omega^2 E_x\left(x,y,z,\omega-\omega_0\right)=0 \qquad (1)
\end{aligned}$$

where $E_x(x,y,z,\omega-\omega_0)$ represents the slowly varying envelope of the optical field. ω_0 is the central frequency of the optical field, μ_0 is the magnetic permeability of vacuum, ε_0 is the electric permittivity of vacuum. $\chi_{xx}^{(1)}$ is the first-order electric susceptibility, describing the fiber dispersion characteristics. $\chi_{xxxx}^{(3)}$ is the third-order electric susceptibility, describing the fiber nonlinear effect.

A. Fiber Dispersion Characteristics Under bending eavesdropping

First, to investigate the impact of fiber dispersion. According to the relationship between fiber refractive index n and first-order electric susceptibility and the weakly guiding approximation in single-mode fiber (SMF).

$$n^2=[1+\chi_{xx}^{(1)}] \qquad (2)$$

$$\beta^2\approx\varepsilon_0\mu_0\left[1+\chi_{xx}^{(1)}\right]\omega^2 \qquad (3)$$

we derive the equivalence relations $\beta^2=\varepsilon_0\mu_0[1+\chi_{xx}^{(1)}]\omega^2=\mu_0\varepsilon_0 n^2\omega^2$. Consequently, Eq. (1) can be simplified to

$$\begin{aligned}
&\frac{\partial^2 E_x(x,y,z,\omega-\omega_0)}{\partial x^2}+\frac{\partial^2 E_x(x,y,z,\omega-\omega_0)}{\partial y^2}+\\
&\frac{\partial^2 E_x(x,y,z,\omega-\omega_0)}{\partial z^2}+\mu_0\epsilon_0 n^2\omega^2 E_x(x,y,z,\omega-\omega_0)=0
\end{aligned} \qquad (4)$$

Under bending eavesdropping, Eq. (4) can be solved via the separation-of-variables method. We assume the solution takes the form:

$$E_x(x,y,z,\omega-\omega_0)=F(x,y)A(z,\omega-\omega_0)e^{j\beta_0 z} \qquad (5)$$

where $A(z,\omega)$ is a slowly varying function of z and β_0 denotes the wavenumber. Eq. (4) separates into two independent equations governing $A(z,\omega)$ and $F(x,y)$, respectively.

$$\left[\frac{\partial^2 F}{\partial x^2}+\frac{\partial^2 F}{\partial y^2}+(\mu_0\epsilon_0 n^2\omega^2-\beta_{be}^2)F\right]Ae^{j\beta_0 z}=0 \qquad (6)$$

$$\left[\frac{\partial^2 A}{\partial z^2}+2j\beta_0\frac{\partial A}{\partial z}+\left(\beta_{be}^2-\beta_0^2\right)A\right]Fe^{j\beta_0 z}=0 \qquad (7)$$

where n_{be} and β_{be} represent the effective refractive index and dispersion under bending eavesdropping. According to $c=1/\sqrt{\varepsilon_0\mu_0}$, $\beta_{be}^2=\mu_0\varepsilon_0 n_{be}^2\omega^2$, Eq. (6) simplifies to

$$\frac{\partial^2 F}{\partial x^2}+\frac{\partial^2 F}{\partial y^2}+\frac{\omega^2}{c^2}(1+\chi_{xx}^{(1)}-n_{be}^2)F=0 \qquad (8)$$

Eq. (7) simplifies to:

$$j\frac{\partial A_x}{\partial z}+\frac{\omega}{c}(n_{be}-n_0)A_x=0 \qquad (9)$$

Eq. (8) and Eq. (9) demonstrate that bending eavesdropping affects the fiber dispersion transmission characteristics by altering parameter n_{be}. Specifically, bending eavesdropping directly influences the fiber dispersion value β_{be} through changes in n_{be}. This introduced β_{be} modifies the amplitude broadening of signals during transmission, thereby providing rich signal features for detecting bending eavesdropping attacks.

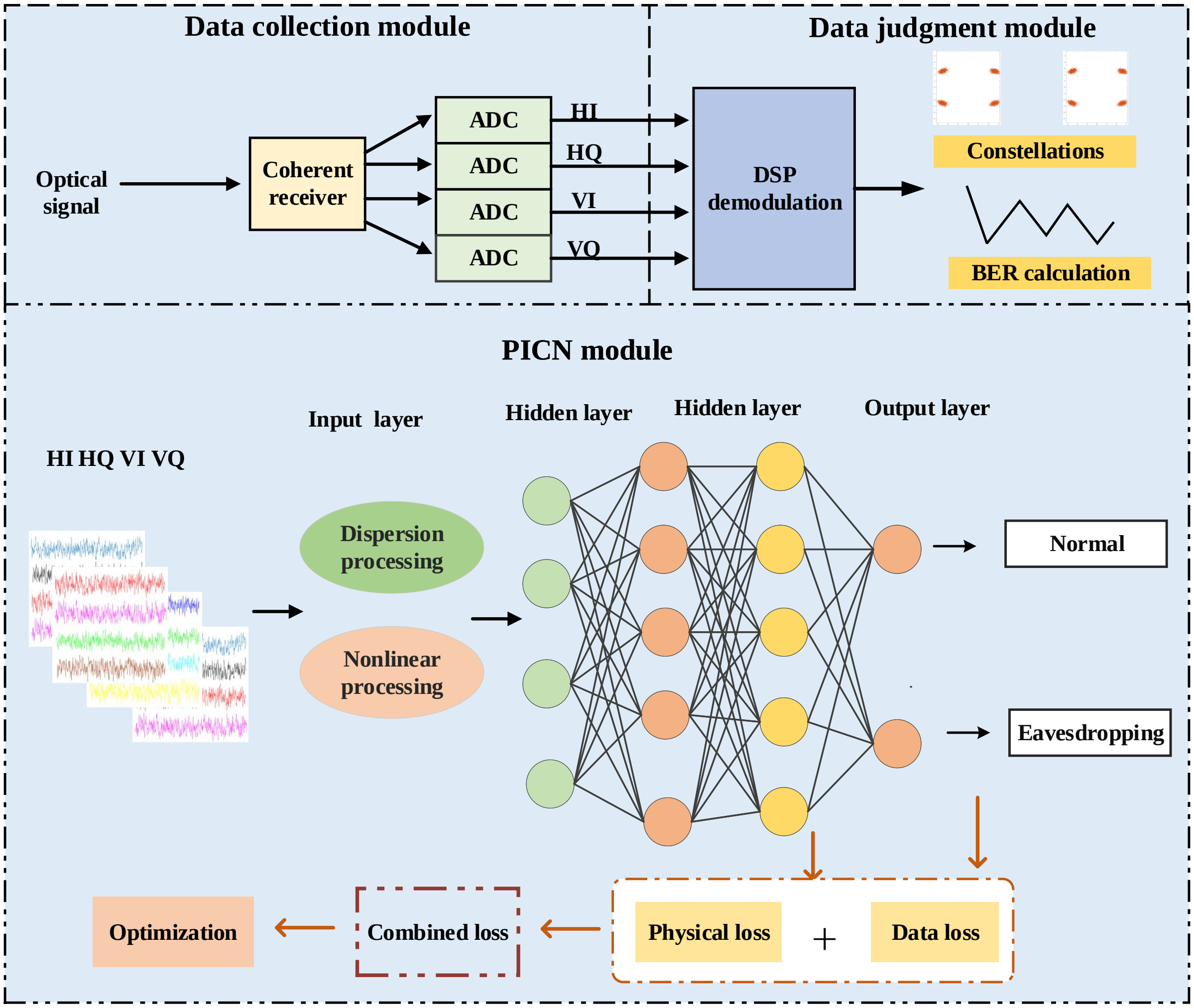

Fig. 1. PICN for bending eavesdropping detection scheme: Data collection module, Data judgment module, PICN module.

B. Nonlinear Effect Under bending eavesdropping

When nonlinear effect is considered, the nonlinear coefficient γ_{be} can be expressed as

$$\gamma_{be} = \frac{\omega_0 \dfrac{3\chi_{xxx}^{(3)}}{4\varepsilon_0 c[1+\chi_{xx}^{(1)}]}}{c\,\dfrac{\left(\iint\limits_{\mathbb{R}^2} |F(x,y)|^2 \mathrm{d}x\mathrm{d}y\right)^2}{\iint\limits_{\mathbb{R}^2} |F(x,y)|^4 \mathrm{d}x\mathrm{d}y}} = \frac{\omega_0 n_2}{cA_{\text{eff}}}$$

$$n_2 = \frac{3\chi_{xxx}^{(3)}}{4\varepsilon_0 c n_{be}^2} \tag{10}$$

In this context, n_2 represents the nonlinear refractive index coefficient and A_{eff} denotes the effective mode area. Eq. (10) demonstrate that bending eavesdropping alters the fiber nonlinear characteristics through modifications to n_{be}. Specifically, bending eavesdropping directly modifies the nonlinear refractive index coefficient n_2 through changes in n_{be}, thereby influencing the parameter γ_{be}. This introduced γ_{be} induces phase variations in the signal transmission, which in turn provides distinctive features for detecting bending eavesdropping.

In summary, bending eavesdropping alters the amplitude and phase of signals by changing the fiber dispersion and nonlinear coefficients. These bending induced amplitude and phase variations are contained in four-channel polarization data. The data structure exhibits analogy to RGB channels in imaging systems, where each channel corresponds to horizontal or vertical polarization. The data value characteristics at each discrete sampling point are analogous to pixels in images. Considering the effect of bending eavesdropping on optical signal transmission and data structure characteristics, a PICN model is proposed. By combining these physical characteristics, the model automatically extracts features related to eavesdropping from the data, achieving high-accuracy detection.

III. BENDING EAVESDROPPING DETECTION SCHEME

A. The PICN model for Bending Eavesdropping

Fig. 1 shows a bending eavesdropping detection scheme based on PICN. The scheme comprises three functional modules, data collection module, data judgment module, and PICN module. In the data collection module, the coherent receiver converts optical signal into electrical signals, which is then sampled by analog-to-digital converter (ADC) to acquire four-channel polarization data (HI, HQ, VI, VQ). The data judgment module is responsible for performing digital signal processing (DSP) on the HI, HQ, VI, VQ, evaluating system performance through constellation diagram analysis and bit error rate (BER). When the BER exceeds the threshold of 3.8×10^{-3}, the HI, HQ, VI, VQ are discarded. Subsequently, the HI, HQ, VI, VQ with BER below the threshold are fed into the PICN module. This module comprises dispersion, nonlinear, and neural network layers. The neural network architecture consists of an input layer, a hidden layer, and an output layer, where the output layer produces classification results indicating normal communication or bending eavesdropping. Note that in the PICN module, to achieve dual constraints of data-driven and physical characteristics, a combined loss function is designed to compute the total loss. The combined loss comprises data loss and physical loss. Specifically, the data loss measures the mismatch between predictions and labels. Meanwhile, the physical loss incorporates dispersion and nonlinear loss, which regulate the model adapts to variations in input amplitude and phase. The optimizer updates the model weights based on the gradients of the total loss, backpropagating the gradients layer by layer through the chain rule. After multiple iterations, the model converges to an optimal parameter configuration. In summary, the proposed scheme realistically simulates the signal propagation process under bending eavesdropping by embedding fiber dispersion and nonlinear effect into CNN. The introduced combined loss function helps to comprehensively capture the features of eavesdropping signals for highly accurate bending eavesdropping detection.

B. Detailed Design of the PICN Model

Next, we detail the architecture of the proposed PICN, illustrated in Fig. 2. The input HI, HQ, VI, VQ first undergo processing through dispersion and nonlinear layers to emulate optical signal propagation. Following this physical preprocessing, a convolutional layer extracts spatially correlated features from the polarized input data. The layer operates by sliding an $f \cdot f$ convolutional kernel across the spatial dimensions of the input with a specified stride. Given the polarization input data X, the feature extraction process can be mathematically formulated as:

$$A_{ij} = \sigma\left(\sum_{p=0}^{f-1}\sum_{q=0}^{f-1} X_{(i\cdot s+p, j\cdot s+p)} \cdot W_{pq} + b\right) \tag{11}$$

where p, q denote the vertical kernel horizontal index of the convolution kernel, σ is the activation function, W represents the weight of the convolution kernel, b is biased, and s denotes stride. The convolution output is processed through the ReLU nonlinear activation function [25] to facilitate learning of both linear and nonlinear data relationships. To improve model generalization and alleviate gradient vanishing during backpropagation, batch normalization is applied between network layers. Finally, the max-pooling layer reduces feature map dimensionality by half, mathematically expressed as:

$$P_{i,j} = \max_{m,n=0}^{f'-1} Z_{i\cdot s'+m, j\cdot s'+n} \tag{12}$$

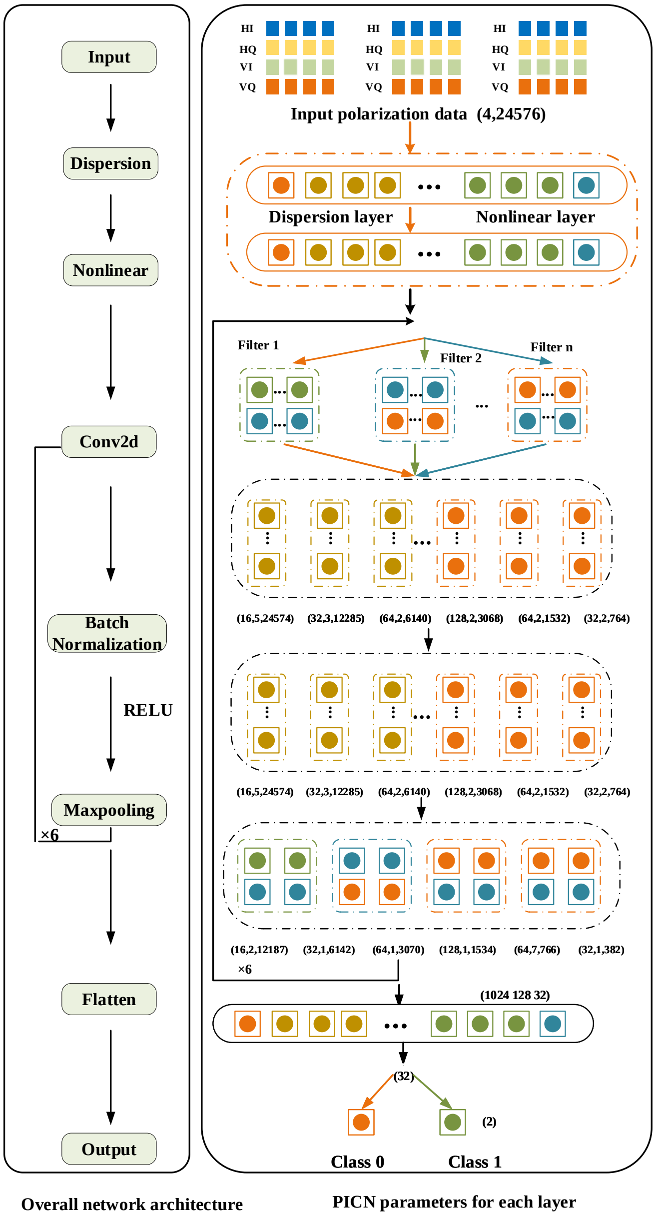

Fig. 2. Parameter settings of the PICN model. polarization data with size of 4×24576, convolutional kernel with size of 2×5, pooling layer with size of 2×2, fully connected layer consisting of 1024, 128, 32, 2.

Following the pooling operation, the extracted features are fed into four fully connected layers to perform binary classification. Class 0 indicates normal communication and Class 1 denotes bending eavesdropping. The specific parameters of the PICN model are as follows, input dimension is 4×24576, convolution kernel 2×5, stride 1×1, pooling 2×2. The combined loss function combines cross-entropy loss [26] and physical loss (dispersion loss, nonlinear effect

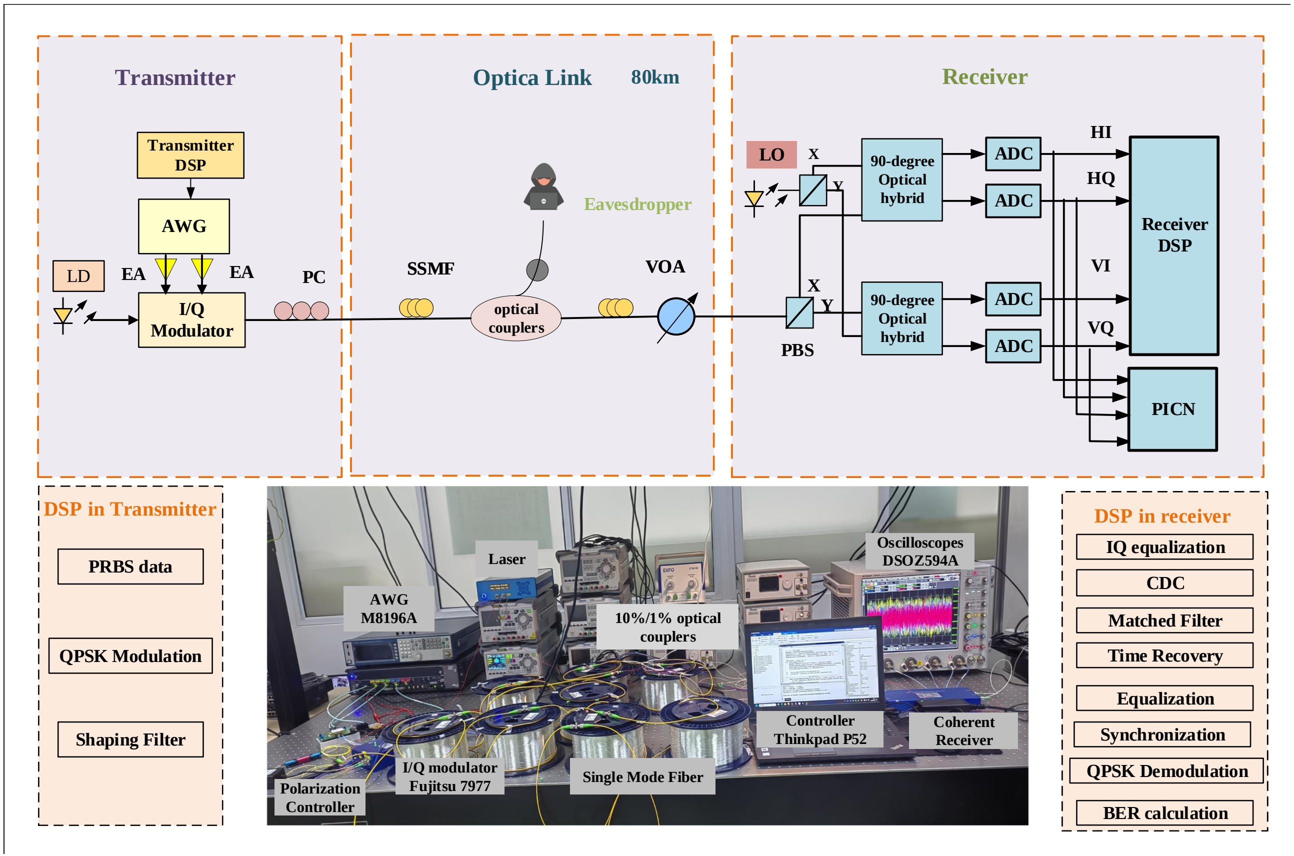

Fig. 3. Experimental step; AWG: Arbitrary waveform generator, LD: Laser diode, EA: Electrical amplifier, IQ-MZM: IQ Mach-Zehnder Modulator, PC: Polarization controller, SSMF: Standard single-mode fiber, VOA: Variable optical attenuator, LO: Local oscillator, PBS: Polarization beam splitter, ADC: Analog-to-digital converter.

loss), as mathematically equations Eq. (13)–(16).

$$\mathcal{L}_{CE} = -\sum_{i=1}^{C} y_c \log(\hat{y}_c) \tag{13}$$

$$\mathcal{L}_{dispersion} = \frac{1}{N}\sum_{i=1}^{N} |\hat{y}_i| \times \lambda_{dispersion} \tag{14}$$

$$\mathcal{L}_{nonlinear} = \frac{1}{N}\sum_{i=1}^{N} \hat{y}_i^2 \times \lambda_{nonlinear} \tag{15}$$

$$\mathcal{L}_{total} = \mathcal{L}_{CE} + \mathcal{L}_{dispersion} + \mathcal{L}_{nonlinear} \tag{16}$$

Here, $\mathcal{L}_{CE}$ represents the cross-entropy loss, and C denotes the total number of classes. Since bending eavesdropping detection is a binary classification task, $C = 2$. y_c represents the polarization data label, which takes values of 0 or 1, and $\hat{y}_c$ denote the predicted probability from the PICN model for normal or bending eavesdropping. $\mathcal{L}_{dispersion}$ represents the dispersion loss, N denotes the batch size. $\hat{y}_i$ are the model's output values, $\lambda_{dispersion}$ is the weight coefficient for the dispersion loss. $\mathcal{L}_{nonlinear}$ represents the nonlinear loss, $\lambda_{nonlinear}$ denotes the weight coefficient for the nonlinear loss, and $\mathcal{L}_{total}$ represents the total loss. To optimize the model, the Adam optimizer is employed during training, which adjusts the model's parameters based on the loss gradients to minimize the discrepancy between predictions and true values.

IV. EXPERIMENTAL SETUP AND DATA COLLECTION

To validate the proposed PICN based bending eavesdropping detection scheme, we establish an 80 km, 168 Gbps dual-polarization QPSK coherent optical communication system, as shown in Fig. 3. At the transmitter, a pseudo-random binary sequence (PRBS) is generated offline that undergoes QPSK modulation and shaping filtering. The processed signals are then loaded into an arbitrary waveform generator (AWG, Keysight M8196A) operating at a sampling rate of 92 GSa/s, which generates I and Q branch signals at a symbol rate of 42 GBaud. Subsequently, the I and Q branch signals are amplified by an electrical amplifier (EA, SHF S807C) and fed into the upper and lower RF ports of the IQ Mach-Zehnder Modulator (IQ-MZM, Fujitsu FTM7977HQA 8V). The light source employs a continuous-wave laser diode (LD) with an output power of 10 mW, a center frequency $f_c = 193.415$ THz, and a linewidth of 100 kHz. After the two branch signals are modulated into optical QPSK signals, the polarization controller adjusts the input polarization states to ensure that each signal can be properly demodulated at the receiving end. The transmission link is based on the G.652.D standard single-mode fiber with a total length of 80 km. To simulate bending eavesdropping [27], we select optical couplers with splitting ratios of 1/99 and 10/90 based on the relationship between the fiber bending power loss coefficient and the bending radius. These couplers simulate bending eavesdropping with radii of 10.8 mm and 15 mm, respectively.

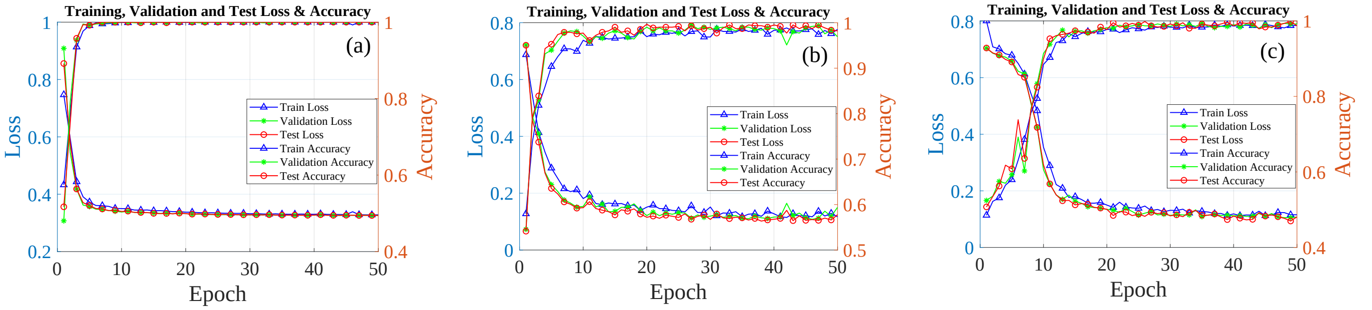

Fig. 4. Learning curves for detection loss and accuracy across the training, validation, and testing phases of the PICN (a) 10.8 mm bending radius, (b) 15 mm bending radius, (c) mixed bending radii.

A variable optical attenuator (VOA) is used to regulate signal output power. At the receiving end, the coherent receiver (U2T CPRV1225A) performs optical-to-electrical conversion, yielding four analog waveforms corresponding to X/Y polarization I/Q components. These signals undergo analog-to-digital conversion via a 4-channel 80 GSa/s oscilloscope (Keysight DSOZ594A), producing digital signals denoted as HI, HQ, VI, VQ. Next, the HI, HQ, VI, VQ signals are processed offline through a series of DSP steps including IQ equalization, chromatic dispersion compensation (CDC), matched filtering, frequency offset estimation (FOE), clock recovery, channel equalization, synchronization, QPSK demodulation, and BER calculation. Finally, digital signals with a BER below the threshold are input into the PICN model for training and testing.

For the datasets of the PICN model, polarization data are initially collected over 80 km fiber links under normal conditions and bending radii of 10.8 mm and 15 mm. Subsequently, the polarization data corresponding to bending radii of 10.8 mm and 15 mm are combined with the normal polarization data to form composite dataset, each containing 4096 polarization data samples. Additionally, to assess PICN model performance under mixed bending radii, a hybrid dataset is constructed by equally allocating 4096 samples from both bending radii. The datasets underwent stratified randomization into training, validation, and test subsets at a 7:1.5:1.5 ratio before being fed into the PICN architecture. Finally, the PICN model is built, trained, and tested using the PyTorch framework.

V. RESULTS AND ANALYSIS

To assess the stability and generalization performance of the PICN model, we first examine the accuracy loss curves across training, validation, and test sets. We then quantitatively investigate the response characteristics of model stability and generalization capability under varying noise intensities and learning rate conditions based on the test set. For comprehensive performance quantification, we employ four quantitative evaluation metrics: Accuracy, Precision, Recall, and F1 Score. These metrics are derived from a confusion matrix, which is a 2 × 2 matrix that describes how well a model predicts bending eavesdropping. The confusion matrix consists of four key elements True Positive (TP), False Positive (FP), True Negative (TN), and False Negative (FN). Where FP denote the number of instances erroneously predicted as the normal class. TP represent the number of instances correctly predicted as the normal class. FN indicate the number of instances incorrectly predicted as the bending eavesdropping class. TN correspond to the number of instances accurately predicted as the bending eavesdropping class. The above four evaluation indicators are calculated using the following formula.

Accuracy is the proportion of the total number of samples for which all predictions are correct.

$$Accuracy = \frac{TP+TN}{TP+TN+FP+FN} \times 100\% \tag{17}$$

Precision is defined as the proportion of true normal samples among those predicted as normal, which measures the model's accuracy in detecting normal cases.

$$Precision = \frac{TP}{TP+FP} \tag{18}$$

Recall represents the proportion of actual normal samples correctly identified, reflecting the model's coverage capability for normal instances.

$$Recall = \frac{TP}{TP+FN} \tag{19}$$

The F1 score is calculated as the harmonic mean of precision and recall, and it comprehensively evaluates the model's balanced prediction performance for normal samples. An increase in this metric typically indicates better equilibrium between prediction accuracy and coverage capability.

$$Accuracy = 2 \times \frac{Precision \times Recall}{Precision + Recall} \tag{20}$$

A. *The Accuracy and Loss curves Analysis of the PICN Model*

Fig. 4(a) illustrates the loss and accuracy curves of the PICN model across the training, validation, and test sets over 50 epochs under the bending radius of 10.8 mm. During the initial 10 epochs, the training set loss decreases and classification accuracy improves from approximately 57% to nearly 100%. Meanwhile, both the validation and test set losses decline as their corresponding classification accuracies rise, indicating strong generalization capability of the model. From epochs 11 to 50, the training, test, and validation sets losses continue to decline steadily until convergence is achieved. Notably, the test set classification accuracy reaches a maximum of 100%.

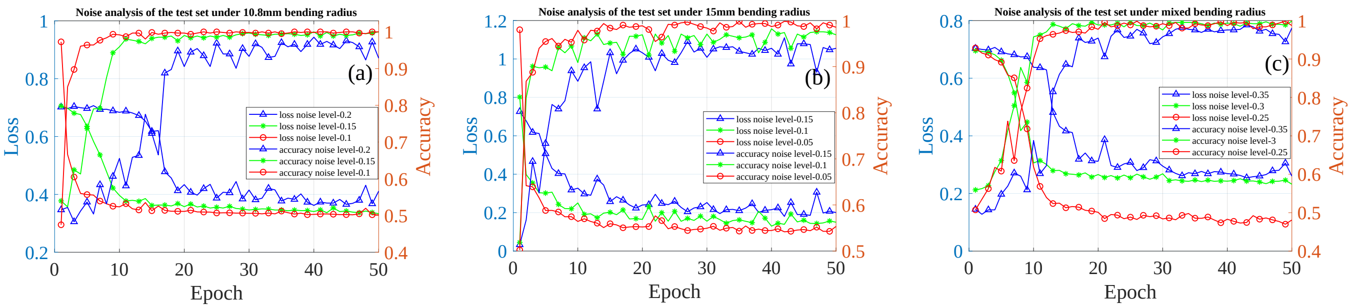

Fig. 5. Noise analysis of the test set under different bending radius (a) 10.8 mm bending radius, (b) 15 mm bending radius, (c) mixed bending radii.

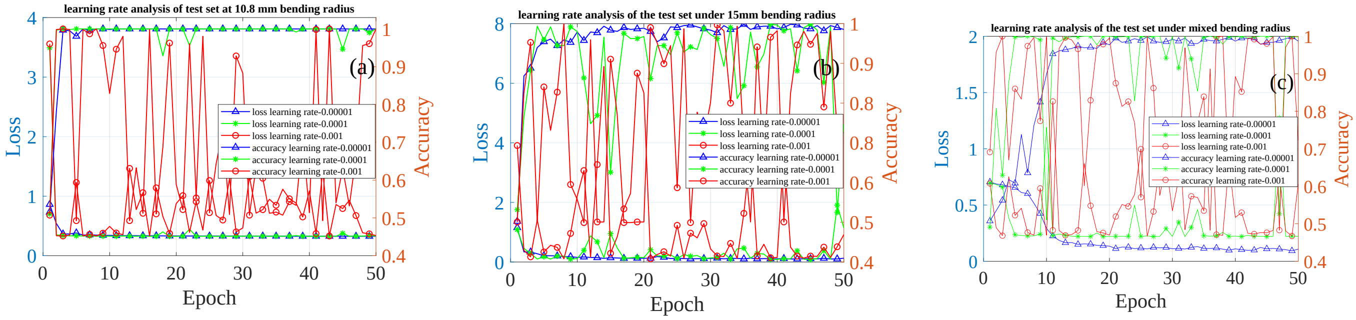

Fig. 6. Learning rate analysis of the test set under different bending radius (a) 10.8 mm bending radius, (b) 15 mm bending radius, (c) mixed bending radii.

Fig. 4(b) presents the loss and accuracy curves of the PICN model across the training, validation, and test sets over 50 epochs under the bending radius of 15 mm. During the first 3 epochs, the training set loss gradually decreases, and the classification accuracy improves from 57.97% to 81.83%, while the validation and test losses also decline and their corresponding accuracies steadily rise. From epochs 4 to 20, the training set loss continues to decrease and the classification accuracy exceeds 98%. Concurrently, the validation and test losses further decrease with their accuracies exceeding 98%, demonstrating enhanced generalization capability. Between epochs 21 and 50, the training, validation, and test set losses remain stable at low levels until final convergence. The test set achieves a peak classification accuracy of 99.67%. These results confirm the PICN model effectively identifies tiny signal changes for single-radius bending eavesdropping detection and demonstrates strong convergence with stable training performance.

Fig. 4(c) illustrates the loss and accuracy curves of the training, validation, and test sets over 50 epochs under mixed bending radii. During the training process, the training set loss decreases from 0.8007 to 0.1123 with its classification accuracy rising from 48.52% to 98.78%, demonstrating the PICN model strong learning capability on the training data. Concurrently, the validation set loss gradually declines as its classification accuracy rises from 52.44% to 98.37%, reflecting enhanced generalization performance. The test set achieves a maximum classification accuracy of 99.84%. These results confirm the PICN model maintains high accuracy for eavesdropping detection across mixed bending radii.

B. Noise Analysis of the Test Set Under Different Bending Radius

Fig. 5(a) evaluates the proposed PICN model's performance across multiple noise levels using test data at a 10.8mm bending radius. At noise levels of 0.1 and 0.15, the model maintains smooth accuracy and loss curves as the epochs increase while achieving 100% accuracy. However, at 0.2 noise level, both metrics exhibit fluctuations accompanied by decreased accuracy. Fig. 5(b) assesses performance at a 15mm bending radius. With 0.05 noise level, smooth accuracy and loss curves persist as the epochs increase, yielding 98.2% accuracy. When noise increases to 0.1, accuracy drops to 96.9%, declining further to 94.6% at 0.15 noise level. Fig. 5(c) examines performance under mixed bending radii. At 0.25 and 0.3 noise levels, stable accuracy and loss curves are maintained with 99.3% accuracy, decreasing to 98.3% at 0.35 noise level. It can be concluded that the PICN model exhibits excellent anti-noise performance under mixed bending radii and its robustness is significantly better than in single bending radius scenarios. This performance requires optimization according to the noise level and bending radius of the actual application scenario.

C. Learning Rate Analysis of the Test Set Under Different Bending Radius

Fig. 6(a) compares and evaluates the proposed PICN model performance under multiple learning rates based on the test set under the bending radius of 10.8 mm. When the learning rate is 0.00001 and 0.0001, both the accuracy and loss of the PICN model remain relatively smooth as the epochs increase, and when the learning rate is 0.001, the changes in

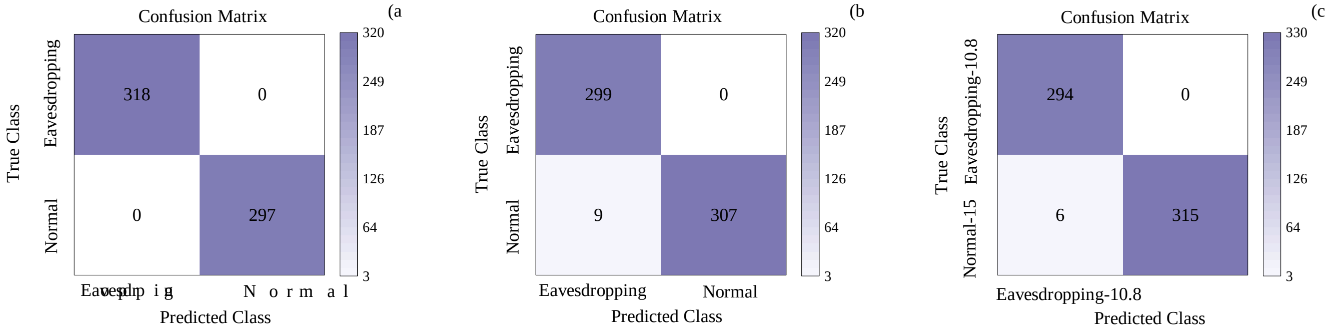

Fig. 7. Confusion matrix for the PICN model (a) 10.8 mm bending radius, (b) 15 mm bending radius, (c) mixed bending radii.

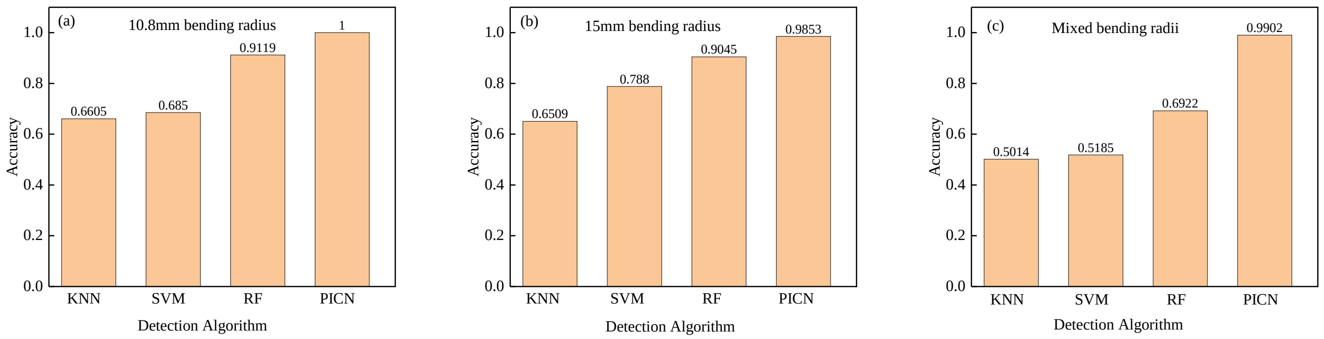

Fig. 8. Detection accuracy comparison of KNN, SVM, RF, and PICN (a) 10.8 mm bending radius, (b) 15 mm bending radius, (c) mixed bending radii.

the accuracy and loss values no longer follow the original linear law. Fig. 6(b) compares and evaluates the proposed PICN model performance under multiple learning rates based on the test set under the bending radius of 15 mm. At a fixed learning rate of 0.00001, both accuracy and loss of the PICN model demonstrate stable convergence characteristics with increasing epochs. When the learning rate rises to 0.0001 or 0.001, however, these metrics exhibit significant nonlinear fluctuations. Fig. 6(c) compares and evaluates the proposed PICN model performance under multiple learning rates based on the test set under the mixed bending radius. The variation patterns of its accuracy and loss align with the conclusions drawn from Fig. 6(a). It can be concluded that as the learning rate decreases, the accuracy and loss curves smooth out and convergence improves. But when the learning rate is 0.0001, the accuracy and loss values at the three bending radii no longer follow the original linear law.

D. Performance Metrics Under PICN Model

Fig. 7(a) presents the confusion matrix for a bending radius of 10.8 mm, achieving 100% accuracy in detecting bending eavesdropping. Fig. 7(b) shows the confusion matrix for a bending radius of 15 mm, achieving 98.53% accuracy in detecting bending eavesdropping. Fig. 7(c) presents the confusion matrix for mixed bending radii, with a detection accuracy of 99.02%. These results show that the PICN model effectively distinguishes between single-radius and mixed bending radii eavesdropping, underscoring its robust capability in detecting.

To verify the effectiveness of the PICN model in bending eavesdropping detection, we compare it with RF, SVM, and KNN. Fig. 8(a) shows that at a bending radius of 10.8 mm, the detection accuracies of KNN, SVM, RF, and PICN reach 66.05%, 68.5%, 91.19%, and 100%, respectively. Fig. 8(b) demonstrates that at a 15 mm bending radius, the detection accuracies become 65.09%, 67.83%, 90.45%, and 98.53%. These results prove the PICN model's outstanding performance in single radius bending eavesdropping detection. Fig. 8(c) shows that under mixed bending radii, the detection accuracies of KNN, SVM, RF, and PICN are 50.14%, 51.85%, 69.22%, and 99.02% respectively. The results demonstrate that PICN achieves optimal performance in eavesdropping detection under mixed bending radii.

In summary, the small variations between bending eavesdropping data and normal data reduce KNN detection accuracy. Furthermore, bending eavesdropping data involves both linear and nonlinear relationships while SVM faces limitations due to feature selection and kernel function constraints. RF relies on data splits for decision making but struggle to capture fine distinctions in intricate nonlinear patterns. In contrast, the PICN model employs deep neural networks to learn input and output relationships and capture subtle feature changes in bending eavesdropping data. Consequently, it achieves the highest accuracy in detecting both single-radius and mixed radii eavesdropping.

Fig. 9(a) illustrates that at a bending radius of 10.8 mm, both bending eavesdropping and normal cases achieve perfect precision, recall, and F1 scores of 1. The PICN model achieves 100% accurate classification with no false positives or negatives. Fig. 9(b) demonstrates that at a bending radius of 15 mm, the normal precision reaches 1, indicating no misclassifications

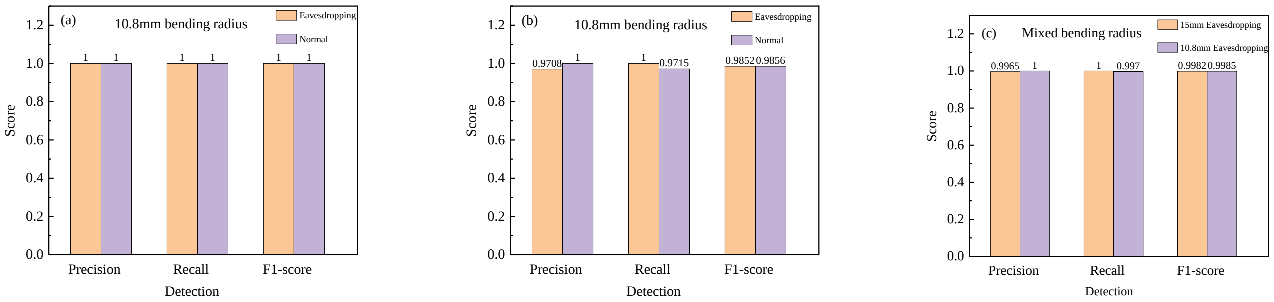

Fig. 9. Precision, Recall, and F1 Score for the PICN model (a) 10.8 mm bending radius, (b) 15 mm bending radius, (c) mixed bending radii.

for normal samples. Furthermore, the bending eavesdropping recall of 1 confirms that all eavesdropping attack samples are correctly classified. The F1 scores of 0.9852 and 0.9856 demonstrate an effective balance between normal precision and attack recall performance. Fig. 9(c) displays the model precision recall and F1 score under mixed bending radii. At a 10.8 mm bending radius the model achieves a precision of 0.98 and recall of 1 with an F1 score of 0.9899. This result shows that the model accurately classifies nearly all eavesdropping attacks. With a 15 mm bending radius precision increases to 1 while recall slightly drops to 0.9813 yielding an F1 score of 0.9906. These results confirm the PICN model precision, recall, and F1 score exhibit dynamic fluctuations across different bending radii. In practical applications we can adjust the model strategy to balance precision recall and F1 score based on specific needs.

VI. CONCLUSION

The feasibility of utilizing the PICN model to detect bending eavesdropping in dual-polarization coherent optical communication systems has been experimentally investigated. First, we establish a theoretical model of optical signal transmission under bending eavesdropping. Building upon this foundation, the PICN model incorporating physical characteristics such as dispersion and nonlinear effect is designed. Subsequently, an experimental platform for bending eavesdropping detection in dual-polarization coherent optical communication systems is established to collect normal polarization data and eavesdropped polarization data. Finally, evaluate and compare the performance of the PICN, RF, SVM, and KNN classifiers in terms of accuracy, precision, recall, and F1 score under both single-radius and mixed radii bending eavesdropping. The experimental results show that PICN achieves detection accuracies of 100%, 98.53%, and 99.02%, under 10.8 mm, 15 mm, and mixed bending radii, respectively. This work validates the feasibility and effectiveness of PICN in detecting bending eavesdropping attacks, while also providing a critical foundation for advancing next-generation intelligent security detection systems.

REFERENCES

[1] X. Gong, Q. Zhang, X. Zhang, R. Xuan, and L. Guo, “Security issues and possible solutions of future-oriented optical access networks for 5g and beyond,” *IEEE Communications Magazine*, vol. 59, no. 6, pp. 112–118, 2021.

[2] Q. Zhang, X. Zhang, X. Gong, and L. Guo, “Crosstalk-avoid virtual optical network embedding over elastic optical networks with heterogeneous multi-core fibers,” *Journal of Lightwave Technology*, vol. 40, no. 24, pp. 7687–7700, 2022.

[3] X. Zhang, C. Xu, H. Zeng, C. Feng, F. Zhang, X. Gong, and L. Guo, “Risk-avoid lightpath provision in space division multiplexing elastic optical data center networks,” *Journal of Lightwave Technology*, 2024.

[4] Q. Zhang, X. Gong, and L. Guo, “Reconfigurable all-optical pattern recognition for psk and qam signals in high-speed optoelectronic firewalls,” *Optics Express*, vol. 32, no. 2, pp. 1736–1755, 2024.

[5] X. Li, Y. Liu, Y. Zhao, Y. Li, Z. Li, S. Rahman, and J. Zhang, “End-to-end service provisioning based on extended segment routing in multi-domain optical networks of f5g,” *Journal of Optical Communications and Networking*, vol. 14, no. 7, pp. 550–561, 2022.

[6] D. Zhang, J. Zhu, X. Liu, X. Wu, J. Li, Y. Zeng, X. Si, and H. Li, “Fiber-to-the-room: a key technology for f5g and beyond,” *Journal of Optical Communications and Networking*, vol. 15, no. 9, pp. D1–D9, 2023.

[7] M. Z. Iqbal, H. Fathallah, and N. Belhadj, “Optical fiber tapping: Methods and precautions,” in *8th international conference on high-capacity optical networks and emerging technologies*. IEEE, 2011, pp. 164–168.

[8] S. Karlsson, M. Andersson, R. Lin, L. Wosinska, and P. Monti, “Detection of abnormal activities on a sm or mm fiber,” in *2023 Optical Fiber Communications Conference and Exhibition (OFC)*. IEEE, 2023, pp. 1–3.

[9] N. Skorin-Kapov, M. Furdek, S. Zsigmond, and L. Wosinska, “Physical-layer security in evolving optical networks,” *IEEE Communications Magazine*, vol. 54, no. 8, pp. 110–117, 2016.

[10] S. Karlsson, R. Lin, L. Wosinska, and P. Monti, “Eavesdropping g. 652 vs. g. 657 fibres: a performance comparison,” in *2022 International Conference on Optical Network Design and Modeling (ONDM)*. IEEE, 2022, pp. 1–3.

[11] V. Spurny, P. Dejdar, A. Tomasov, P. Munster, and T. Horvath, “Eavesdropping vulnerabilities in optical fiber networks: investigating macro-bending-based attacks using clip-on couplers,” in *2023 International Workshop on Fiber Optics on Access Networks (FOAN)*. IEEE, 2023, pp. 47–51.

[12] K. Shaneman and S. Gray, “Optical network security: technical analysis of fiber tapping mechanisms and methods for detection & prevention,” in *IEEE MILCOM 2004. Military Communications Conference, 2004.*, vol. 2. IEEE, 2004, pp. 711–716.

[13] T. D. Bradley, M. Van Den Hout, B. Kalla, V. Van Vliet, M. Bigot-Astruc, A. A. Correa, P. Sillard, G. Weiner, P. Winzer, and C. Okonkwo, “Fiber eavesdropping using tapers in standard and trench-assisted single-mode fibers,” *IEEE Photonics Technology Letters*, 2024.

[14] T. Uematsu, H. Hirota, T. Kawano, T. Kiyokura, and T. Manabe, “Design of a temporary optical coupler using fiber bending for traffic monitoring,” *IEEE Photonics Journal*, vol. 9, no. 6, pp. 1–13, 2017.

[15] K. Noto, T. Uematsu, H. Iida, C. Fukai, and I. Ogushi, “Threshold design in fiber termination identification using local injection and otdr,” *Optical Fiber Technology*, vol. 81, p. 103497, 2023.

[16] W. Qin, Q. Zhang, W. Hou, X. Zhang, and X. Gong, “Convolutional neural networks for fiber-bending eavesdropping attacks detection in

coherent optical communication systems," in *2024 International Conference on Ubiquitous Communication (Ucom)*. IEEE, 2024, pp. 342–345.

[17] L. Sadighi, S. Karlsson, C. Natalino, and M. Furdek, "Machine learning-based polarization signature analysis for detection and categorization of eavesdropping and harmful events," in *2024 Optical Fiber Communications Conference and Exhibition (OFC)*. IEEE, 2024, pp. 1–3.

[18] L. Sadighi, S. Karlsson, C. Natalino, L. Wosinska, M. Ruffini, and M. Furdek, "Deep learning for detection of harmful events in real-world, noisy optical fiber deployments," *Journal of Lightwave Technology*, 2025.

[19] H. Song, R. Lin, L. Wosinska, P. Monti, Y. Li, and J. Zhang, "Eavesdropping detection and localization in wdm optical system," in *2023 IEEE Future Networks World Forum (FNWF)*. IEEE, 2023, pp. 1–5.

[20] Y. Li, L. Yuyuan, M. Zhang, S. Wei, Z. Huatao, Y. Li, Y. Zhao, and J. Zhang, "Fiber eavesdropping detection and location in optical communication system," in *Photonics*, vol. 12, no. 5. MDPI AG, 2025, p. 501.

[21] H. Song, R. Lin, Y. Li, Q. Lei, Y. Zhao, L. Wosinska, P. Monti, and J. Zhang, "Machine-learning-based method for fiber-bending eavesdropping detection," *Optics Letters*, vol. 48, no. 12, pp. 3183–3186, 2023.

[22] H. Song, Y. Li, M. Liu, K. Wang, J. Li, M. Zhang, Y. Zhao, and J. Zhang, "Experimental study of machine-learning-based detection and location of eavesdropping in end-to-end optical fiber communications," *Optical Fiber Technology*, vol. 68, p. 102669, 2022.

[23] X. Gong, M. Zhou, Q. Zhang, J. Pang, and L. Guo, "Experimental demonstration of optical eavesdropping detection based on the backpropagation neural network for coherent optical communication systems," in *2022 Asia Communications and Photonics Conference (ACP)*. IEEE, 2022, pp. 491–494.

[24] G. P. Agrawal, *Fiber-optic communication systems*. John Wiley & Sons, 2012.

[25] V. Nair and G. E. Hinton, "Rectified linear units improve restricted boltzmann machines," in *Proceedings of the 27th international conference on machine learning (ICML-10)*, 2010, pp. 807–814.

[26] T. Fushiki, "Estimation of prediction error by using k-fold cross-validation," *Statistics and Computing*, vol. 21, pp. 137–146, 2011.

[27] W. Qin, X. Gong, W. Hou, T. Zhang, X. Zhang, and L. Guo, "Convolutional neural network for detecting fiber-bending eavesdropping attacks in optical communication systems," *Optics Express*, vol. 33, no. 10, pp. 20 894–20 906, 2025.

Wenshuai Qin received an M.S. degree in 2021 from Shanxi University, Shanxi, China, where he is currently working toward the Ph.D. degree in Chongqing University of Posts and Telecommunications, Chongqing, China. His research interests include machine learning, fiber nonlinear, optical signal processing, and secure optical transmission system.

Xiaoxue Gong (Member, IEEE) received her B.S. degree in 2011, M.S. degree in 2013, and Ph.D. degree in 2017 from Northeastern University, Shenyang, China. During 2016–2017, she conducted academic research at Bangor University, United Kingdom. She is currently a professor in the School of Communication and Information Engineering, Chongqing University of Posts and Telecommunications, China. Her research interests include optical communication, optical signal processing, optical access networks, and network optimization.

Weigang Hou (Member, IEEE) received the Ph.D. degree in information and communication system from Northeastern University, Shenyang, China, in 2013. In 2012, he was an Associate Researcher with the Department of Computer Science, City University of Hong Kong, Hong Kong. He is currently a Full Professor with the Chongqing University of Posts and Telecommunications, Chongqing, China. He holds more than 120 publications. Among these, more than 80 papers are published as the first/corresponding author, and they span IEEE magazine, trans, journals, and some famous conferences. His research focuses on the area of optical networks on chips.

Lu Gan (Senior Member, IEEE) received the B.Eng. and M.Eng. degrees from South East University, Nanjing, China, in 1998 and 2000, respectively, and the Ph.D. degree from Nanyang Technological University, Singapore, in 2004.,She is currently a Senior Lecturer (Associate Professor) with Brunel University London, Uxbridge, U.K. She has been on the faculties of the University of Newcastle, Callaghan, NSW, Australia, from 2004 to 2006, and the University of Liverpool, Liverpool, U.K, from 2006 to 2007. Her research interests include fundamental signal processing theories and their applications in image/video coding and processing, nondestructive terahertz and ultrasound imaging, machine learning, and wireless communications. Dr. Gan was a Technical Committee Member for conferences, including the IEEE International Conference on Acoustics, Speech and Signal Processing (ICASSP), the IEEE International Conference on Image Processing (ICIP), and Globecom. She is a reviewer for research grants of the Engineering and Physical Sciences Research Council (EPSRC), the Science and Technology Facilities Council (STFC), the Research Foundation Flanders (FWO), and many top journals including IEEE Transactions on Information Theory, IEEE Transactions on Signal Processing, IEEE Transactions on Communications, and IEEE Transactions on Image Processing. She serves as an Associate Editor for the IEEE Signal Processing Letters.

Lei Guo (Senior Member, IEEE) received his Ph.D. from the University of Electronic Science and Technology of China in 2006. He is a professor at Chongqing University of Posts and Telecommunications, Chongqing, China. His current research interests include communication networks, optical communications, and wireless communications. He has published over 200 technical papers in the above areas in international journals and conferences, such as the IEEE Transactions on Communications, the IEEE Transactions on Wireless Communications, the IEEE/OPTICA Journal of Lightwave Technology, the IEEE/OPTICA Journal of Optical Communications and Networking, the IEEE GLOBECOM, and the IEEE ICC. He is a member of IEEE and OPTICA, and he is also a senior member of CIC. He is now serving as an editor for five international journals.